Supplementary Information

Unconventional Low Temperature Decomposition of a Saturated Hydrocarbon over Atomically-Dispersed Titanium-Aluminum-Boron Catalyst

Souvick Biswas[1,⫣], Jack Cokas[2,⫣], Winston Gee[2], Dababrata Paul[1], Nureshan Dias[3], Harry W. T. Morgan[2], Matthew T. Finn[4], Bethany M. Hudak[5], Perrin M. Godbold[6], Christopher A. Klug[4], Albert Epshteyn[4*], Anastassia N. Alexandrova[2*], Musahid Ahmed[3*], Ralf I. Kaiser[1*]

[1] Department of Chemistry, University of Hawai'i at Manoa, Honolulu, Hawaii 96822, United States

[2] Department of Chemistry and Biochemistry, University of California, Los Angeles, Los Angeles, California 90095, United States

[3] Chemical Sciences Division, Lawrence Berkeley National Laboratory, Berkeley, California 94720, United States

[4] Chemistry Division, U.S. Naval Research Laboratory, Washington, D.C. 20375, United States

[5] Materials Science and Technology Division, U.S. Naval Research Laboratory, Washington, DC, 20375, United States

[6] NRC Postdoctoral Associate, Chemistry Division, U.S. Naval Research Laboratory, Washington, DC 20375, United States
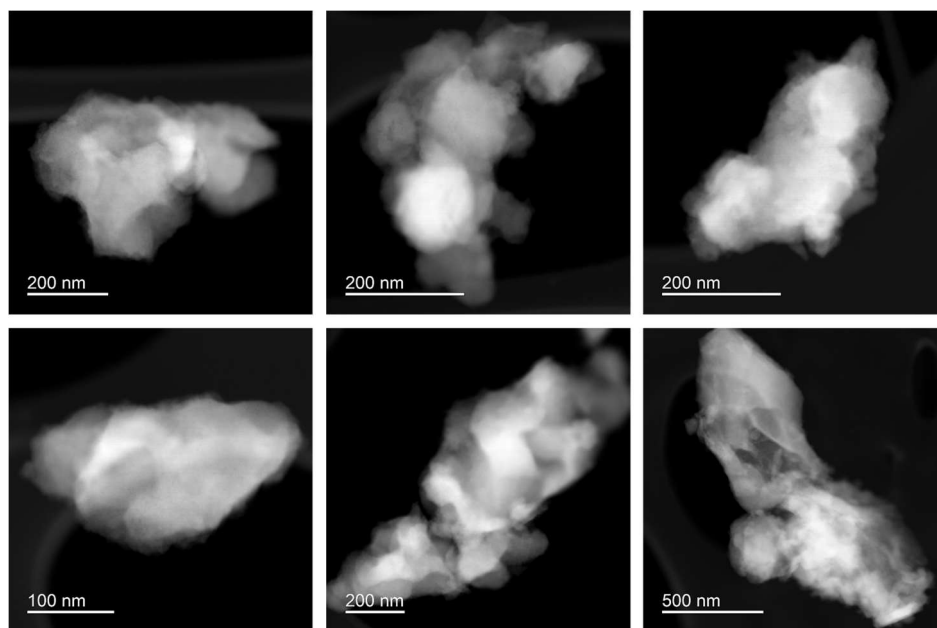
* Corresponding author. E-mail: albert.epshteyn@nrl.navy.mil
        ana@chem.ucla.edu
        mahmed@lbl.gov
        ralfk@hawaii.edu

⫣ These authors contributed equally

Supplementary Fig. 1: Microscopic images of TiAlB NP. The high-angle annular dark-field (HAADF) scanning transmission electron microscopy (STEM) images of titanium-aluminum-boron nanopowder (TiAlB NP).

Supplementary Table 1: List of peaks in the Raman spectrum of the TiAlB nanopowder and their assignments.

Peak	Experimental wavenumber (cm^{-1})	Literature wavenumber (cm^{-1})	Assignment / carrier
1	142	144	O−Ti−O bending[1]
2	157	161	Ti−Al−B bending[2] (deformation of weaker Ti−Al bond)
3	226	227	Ti−Al stretching[2]
4	257	252 242	Ti−Al−B bending (shear vibration)[2] B−Al−B bending[3]
5	414	410	Ti−B stretching[4]
6	489	488	Al−B stretching[3]
7	609	610	Ti−B−Al bending / phonon mode[2] (deformation of stronger Ti−B bond)
8	898	883	Phonon mode of TiB$_2$ phase[4]

Supplementary Discussion 1. X-ray photoelectron spectroscopy (XPS) of TiAlB NP:

The TiAlB NP was directly pressed with a spatula into indium foil and mounted via copper pins into the sample holder. Analysis was conducted with a ThermoFisher Nexsa Surface Analysis System. At least 16 scans were conducted for each high-resolution spectrum. The flood gun was used to minimize sample charging, and the signals were normalized to adventitious carbon at 284.8 eV. For peak fitting Shirley backgrounds were used. B and Al were fitted with Avantage software and Ti was fitted with both Avantage and CasaXPS.
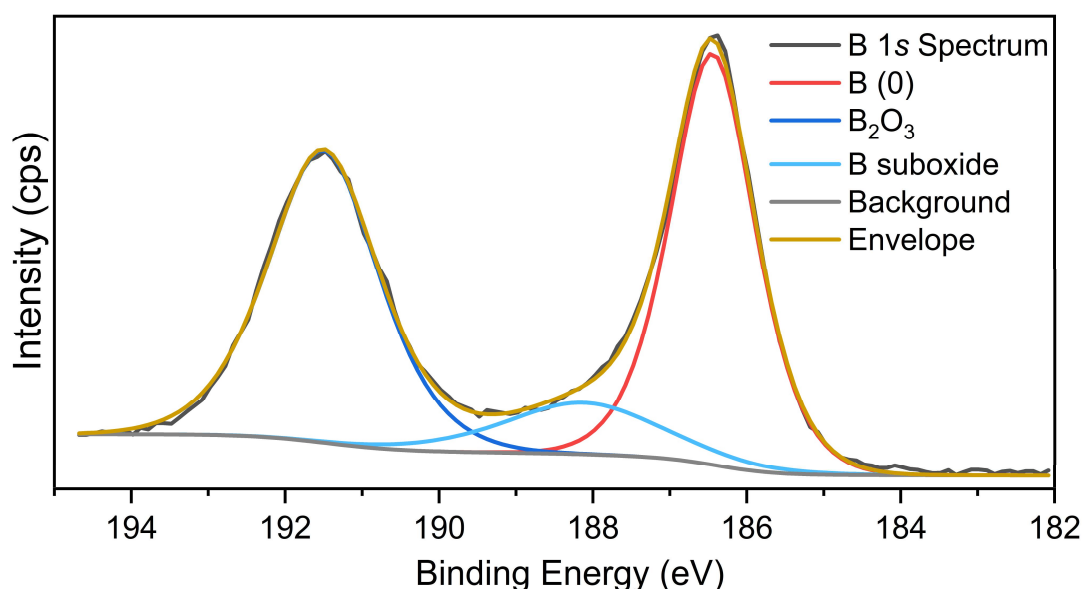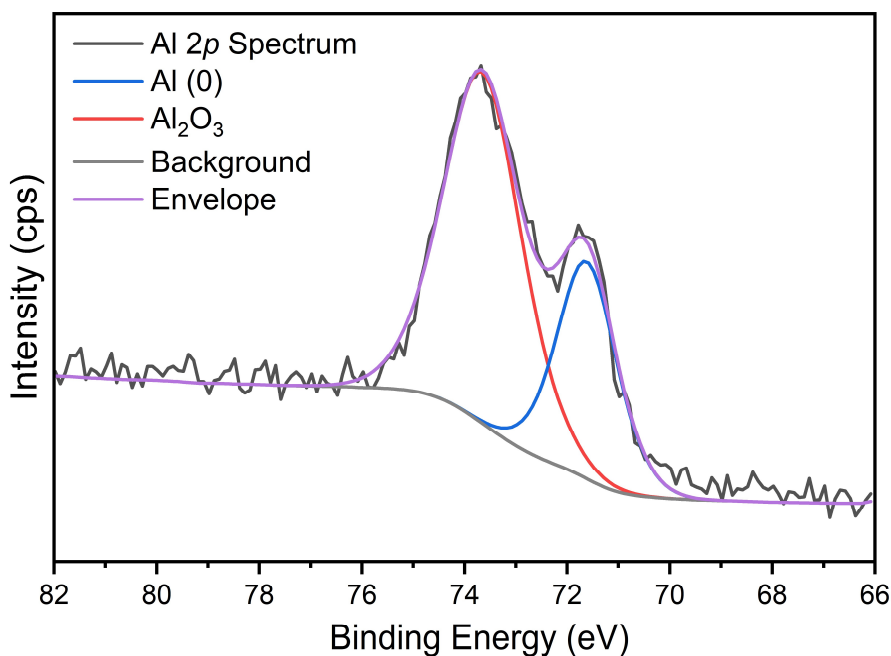

Supplementary Fig. 2: Deconvoluted B 1s spectrum for TiAlB NP with normalized chi-square value of 1.4. The experimental spectrum is presented by the *black* trace, while the following color code is used for fitting different traces. *Red*: elemental boron, *blue*: diboron trioxide (B_2O_3), *sky blue*: boron suboxide, *grey*: background, *golden yellow*: envelope.

Supplementary Fig. 2 shows the B 1s spectrum with three fitting features: primarily, elemental B with a nominal oxidation of (0) at a binding energy of 186.4 eV along with a feature of B_2O_3 or B(III) at 191.5 eV. These are both lower than anticipated and possibly due to the different rates of charging between the adventitious carbon and the metallic NP. The broad

feature between the two peaks is the suboxide which transitions between the two states of the elemental boron and the passivated boron.
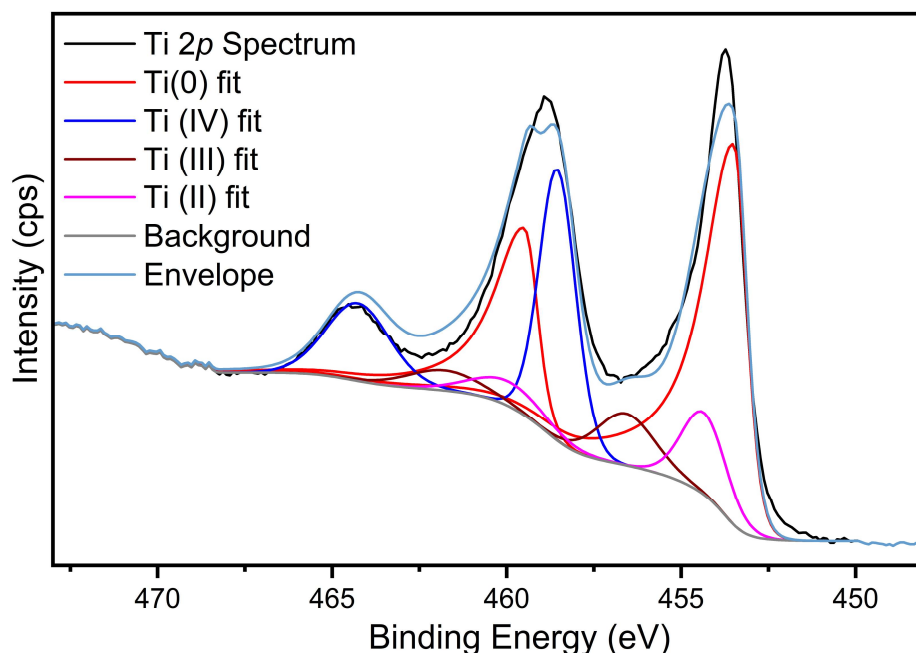
The deconvoluted Al 2*p* spectrum (Supplementary Fig. 3) shows two peaks attributed to elemental Al and Al_2O_3. Notably, the ratio of Al_2O_3 to metallic Al is reasonable and typical of a passivation Al layer though the separation between the two peaks is less than expected suggesting the oxidation states are closer together than simply +3 to 0. The shoulder around 70 eV suggests a spilt metal state, possibly from different bonding environments such as Al-B and Al-Ti linkages. Notice that our theoretical model does not include the surface passivation, under the assumption that in reaction conditions the trace oxide gets reduced.


Supplementary Fig. 3: Deconvoluted Al 2*p* spectrum for TiAlB NP with normalized chi-square value of 1.4. The experimental spectrum is presented by the *black* trace, while the following color code is used for fitting different traces. *blue*: elemental aluminum, *red*: aluminum trioxide (Al_2O_3), *grey*: background, *light purple*: envelope.

The Ti 2*p* spectrum is substantially less simple. Supplementary Fig. 4 shows the spectrum with an imperfect fit (STD residual of 7). Because a fit did not converge even with generous

relaxing of literature values, the fit shown is one which preserves the literature standards for peak position, peak shape, FWHM, and doublet spacing.[5-8] Ti(0) exists in abundance and may be key to an appropriate fit. It was fitted with its characteristic asymmetric peak shape (LA(1.1,5,7)). The overall fit seems to under fit on the right (the metallic side, simply comparing the envelope and the raw spectrum). However, when intensity matching was attempted, the left side became overfit, as the doublets ($2p_{1/2}$) are half the integrated counts of the main features ($2p_{3/2}$). More work and analysis could be done to resolve instrumental and chemical abnormality of this sample and spectrum but the fit as is still provides the basic chemical information: Even with this imperfect fit, it is clear to see that all four oxidation states are present (Ti(0), Ti(II), Ti(III), and Ti (IV)) with predominant abundances of Ti(0) and little contributions from the suboxides, or perhaps in this case partial surface oxides.


Supplementary Fig. 4: Deconvoluted Ti 2p spectrum for TiAlB NP. The experimental spectrum is presented by the *black* trace, while the following color code is used for fitting different traces. *Red*: elemental titanium [Ti(0)], *blue*: Ti(IV), *wine red*: Ti(III), *pink*: Ti(II), *grey*: background, *ocean blue*: envelope.
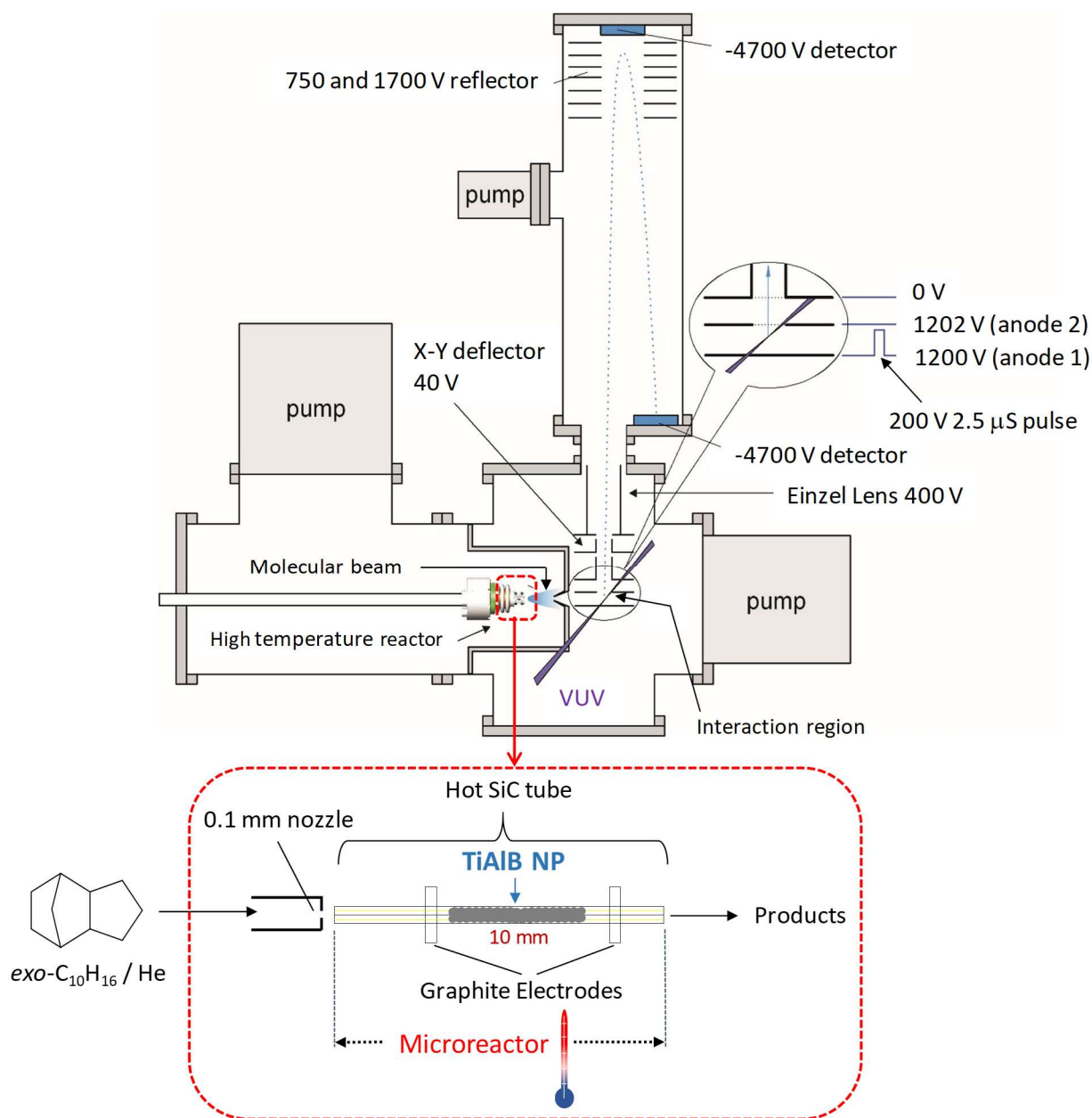
Supplementary Fig. 5: Schematic of the catalytic microreactor-coupled molecular beam machine. Full experimental setup including high temperature microreactor (magnified rectangular section in red) and reflectron time-of-flight mass spectrometer (Re-TOF-MS) for probing the catalysis.[9] Reprinted (adapted) with permission from Biswas, S., Paul, D., Dias, N., Lu, W., Ahmed, M., Pantoya, M. L., Kaiser, R. I. Efficient oxidative decomposition of jet-fuel *exo*-tetrahydrodicyclopentadiene (JP-10) by aluminum nanoparticles in a catalytic microreactor: An online vacuum ultraviolet photoionization study. *J. Phys. Chem. A* **128**, 1665-1684 (2024). Copyright 2024 American Chemical Society.
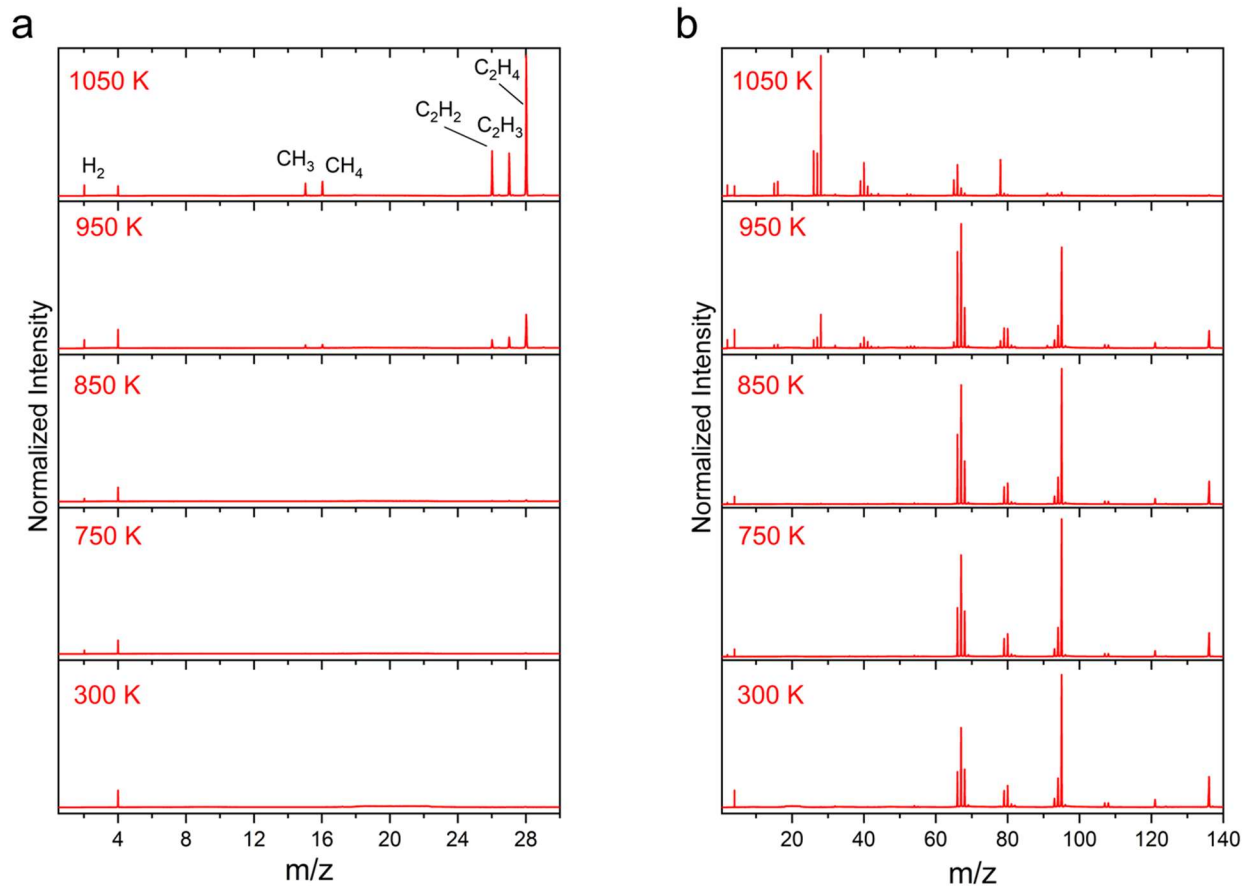
Supplementary Fig. 6: Photoionization mass spectra of catalyically decomposed products at 15.4 eV. Mass spectra of the products formed upon decomposition of helium-seeded *exo*-tetrahydrodicyclopentadiene (*exo*-$C_{10}H_{16}$) over titanium-aluminum-boron nanopowder (TiAlB NP) recorded at a photon energy of 15.4 eV in the 300-1050 K temperature range for m/z upto (a) 30 amu and (b) 140 amu.
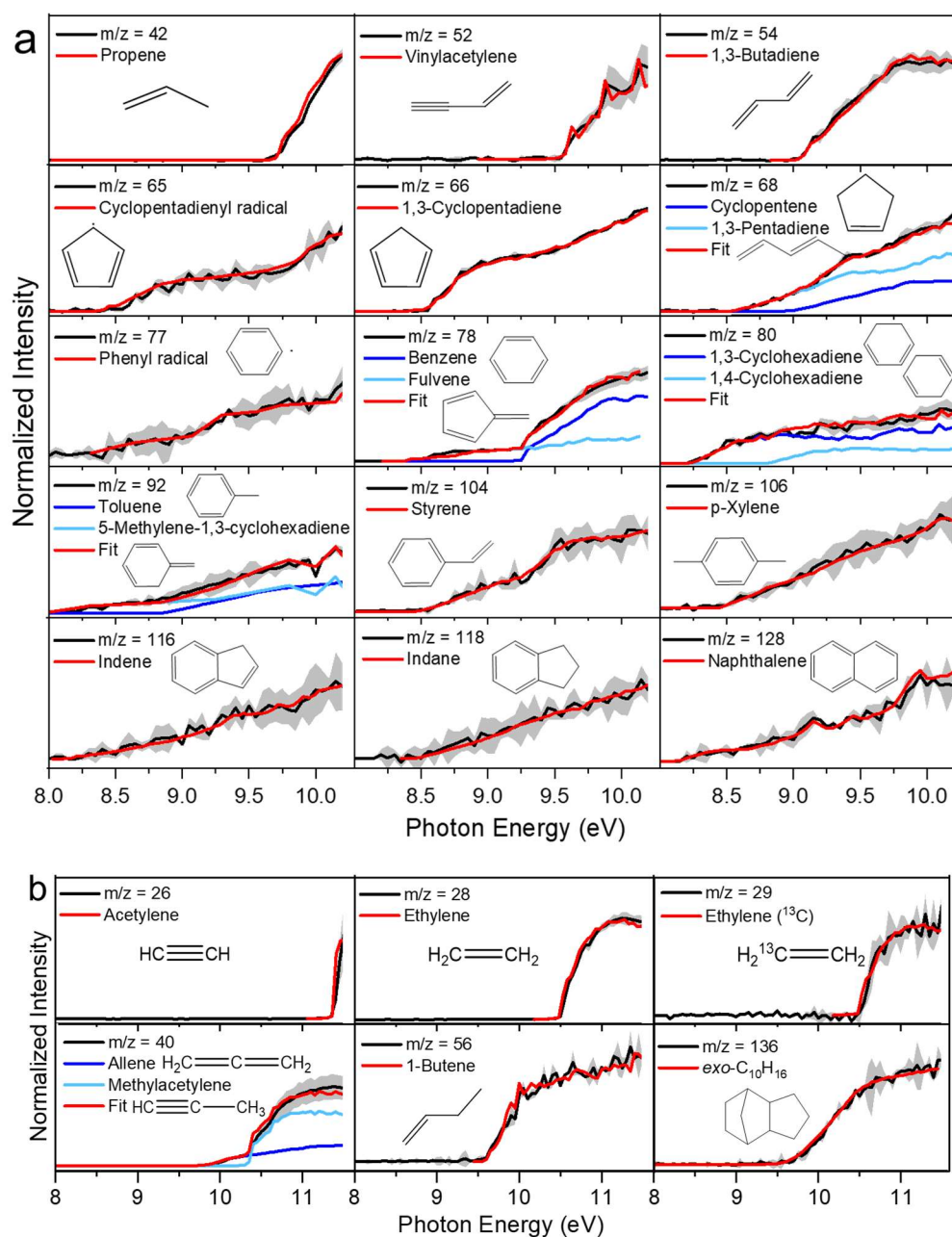
Supplementary Fig. 7: PIE curves and product identification at 1050 K. Experimental photoionization efficiency curves (PIE, *black* traces) in the range of (a) 8.0 - 10.2 eV and (b) 8.0 - 11.5 eV for the products at distinct mass-to-charge ratios at 1050 K. The experimental errors (*gray* shaded area) originate from the accuracy of the photocurrent measurement by the photodiode and a 1σ error of the PIE curves averaged over the individual scans. In case of multiple isomers, reference PIE curves are represented as *royal* and *sky blue* traces; the overall fit is depicted in a *red* trace, whereas for a single species contributing to a mass peak, the reference trace is solely represented by the *red* trace.
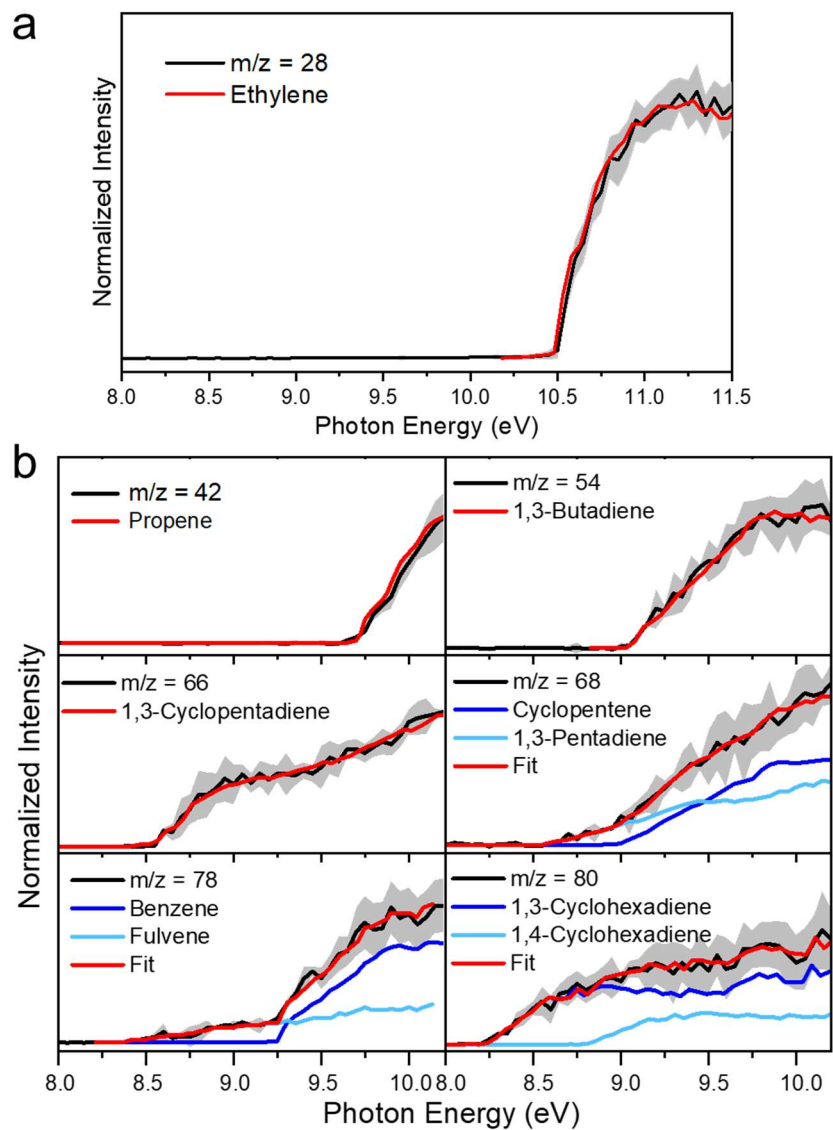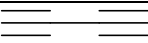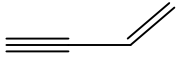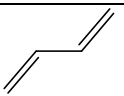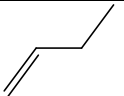
Supplementary Fig. 8: PIE curves and product identification at 850 K. Experimental photoionization efficiency curves (PIE, *black* traces) for (a) m/z = 28 and (b) m/z = 42, 54, 66, 68, 78 and 80 upon decomposition of helium-seeded *exo*-tetrahydrodicyclopentadiene (*exo*-$C_{10}H_{16}$) over titanium-aluminum-boron nanopowder (TiAlB NP) at 850 K. The experimental errors (*gray* shaded area) originate from the accuracy of the photocurrent measurement by the photodiode and a 1σ error of the PIE curves averaged over the individual scans. In case of multiple isomers, reference PIE curves are represented as *royal* and *sky blue* traces; the overall fit is depicted in a *red* trace, whereas for a single species contributing to a mass peak, the reference trace is solely represented by the *red* trace.
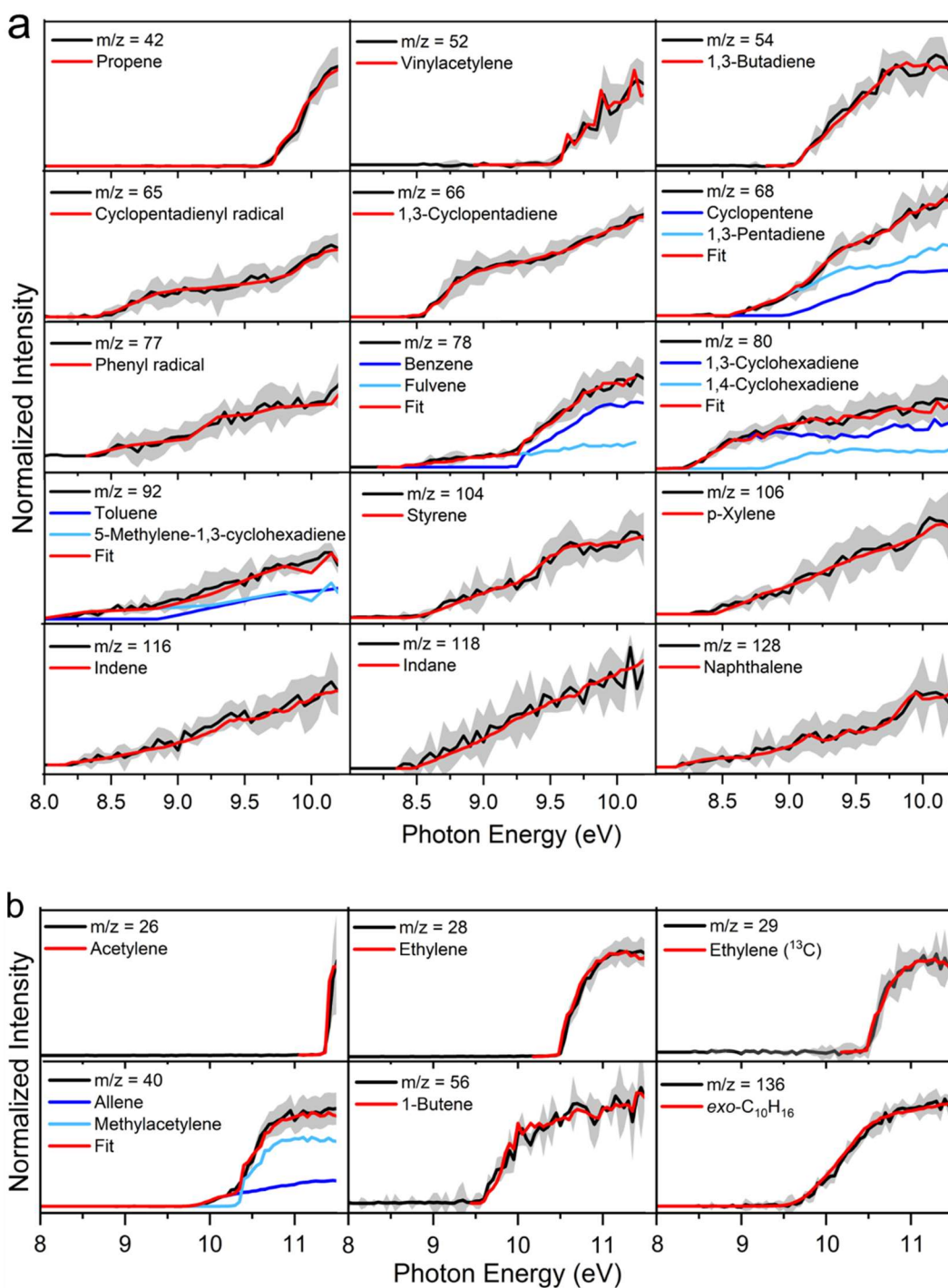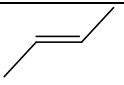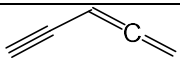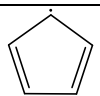
Supplementary Fig. 9: PIE curves and product identification at 950 K. Experimental photoionization efficiency curves (PIE, *black* traces) in the range of (a) 8.0 - 10.2 eV and (b) 8.0 - 11.5 eV for distinct mass-to-charge ratios upon decomposition of helium-seeded *exo*-tetrahydrodicyclopentadiene (*exo*-$C_{10}H_{16}$) over titanium-aluminum-boron nanopowder (TiAlB NP) at 950 K. The experimental errors (*gray* shaded area) originate from the accuracy of the
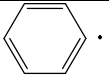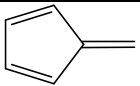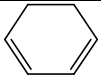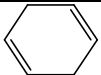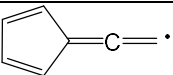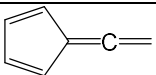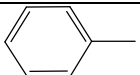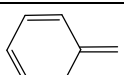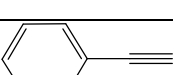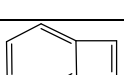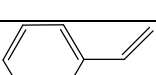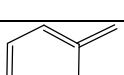
photocurrent measurement by the photodiode and a 1σ error of the PIE curves averaged over the individual scans. In case of multiple isomers, reference PIE curves are represented as *royal* and *sky blue* traces; the overall fit is depicted in a *red* trace, whereas for a single species contributing to a mass peak, the reference trace is solely represented by the *red* trace.
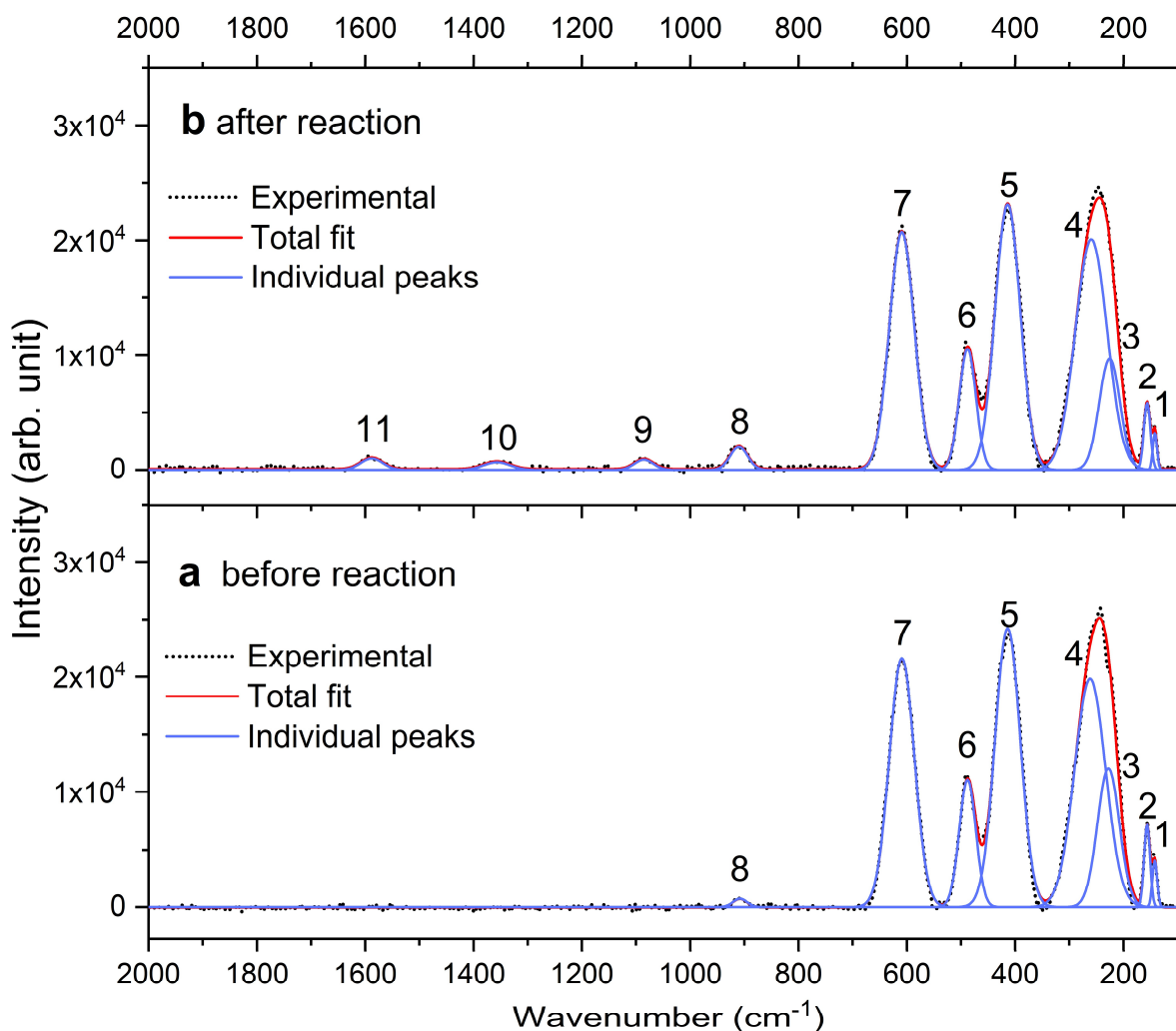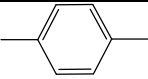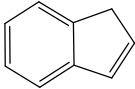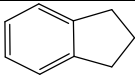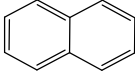
Supplementary Fig. 10: Raman spectral changes of TiAlB NP after catalysis. Deconvoluted micro-Raman spectra of the TiAlB nanopowder excited with 532 nm laser (a) before and (b) after the catalysis. The experimental spectra are depicted by *black* dotted line, whereas individual fitted peaks and total fits are *indigo* and *red* colored solid lines, respectively. Peaks 10 (1357 cm^{-1}) and 11 (1588 cm^{-1}) are the features of graphitic substance - *D*-band and *G*-band respectively.[10,11] Peak 9 can be assigned to B−C stretching in B_4C.[4]

Supplementary Table 2: Mass, molecular formula, name, and structure of the individual products formed in the decomposition of helium-seeded *exo*-tetrahydrodicyclopentadiene (*exo*-$C_{10}H_{16}$) with and without TiAlB reactive mixed-metal nanopowder inside the microreactor.

Mass	Molecular formula	Name	Structure	*exo*-$C_{10}H_{16}$/ He[12]	*exo*-$C_{10}H_{16}$/ He/TiAlB
2	H_2	Hydrogen	H-H	+	+
15	CH_3	Methyl	$CH_3^{\bullet}$	+	-
16	CH_4	Methane	CH_4	-	+
26	C_2H_2	Acetylene	HC≡CH	+	+
27	C_2H_3	Vinyl	$H_2C=CH^{\bullet}$	+	-
28	C_2H_4	Ethylene	$H_2C=CH_2$	+	+
29	C_2H_5	Ethyl	$H_3C-CH_2^{\bullet}$	+	-
39	C_3H_3	Propargyl	$HC≡C-CH_2^{\bullet}$	+	-
40	C_3H_4	Allene	$H_2C=C=CH_2$	+	+
		Methylacetylene	$HC≡C-CH_3$	+	+
41	C_3H_5	Allyl	$H_2C=CH-CH_2^{\bullet}$	+	-
42	C_3H_6	Propene	$H_2C=CH-CH_3$	+	+
50	C_4H_2	Diacetylene	≡—≡	+	-
52	C_4H_4	Vinylacetylene	≡—⁄	+	+
		1,2,3-Butatriene	=C=C=	+	-
54	C_4H_6	1,3-Butadiene	⁄⁄	+	+
56	C_4H_8	1-Butene	⁄⁄	+	+
		2-Butene	⁄=	+	-
64	C_5H_4	Ethynylallene	≡C=	+	-
65	C_5H_5	Cyclopentadienyl	(cyclopentadienyl ring)	+	+

66	C_5H_6	1,3-Cyclopentadiene		+	+
68	C_5H_8	Cyclopentene		+	+
		1,3-Pentadiene	$H_2C=CH-\overset{H}{C}=CH-CH_3$	+	+
77	C_6H_5	Phenyl		-	+
78	C_6H_6	Benzene		+	+
		Fulvene		+	+
80	C_6H_8	1,3-Cyclohexadiene		+	+
		1,4-Cyclohexadiene		+	+
82	C_6H_{10}	Cyclohexene		+	-
89	C_7H_5	Fulvenallenyl		+	-
90	C_7H_6	Fulvenallene		+	-
92	C_7H_8	Toluene		+	+
		5-Methylene-1,3-cyclohexadiene		+	+
102	C_8H_6	Phenylacetylene		+	-
		Benzocyclobutene		+	-
104	C_8H_8	Styrene		+	+
		o-Xylylene		+	-

106	C_8H_{10}	p-xylene		+	+
		1,3,5-Cyclooctatriene		+	-
116	C_9H_8	Indene		+	+
118	C_9H_{10}	Indane		+	+
128	$C_{10}H_8$	Naphthalene		-	+

Supplementary Discussion 2. Branching ratio determination: In order to calculate the branching ratios of the products, the following relationship between the integrated ion intensity of species i, $(S_i(T,E))$ normalized by photon flux, the mole fraction $X_i(T)$, the photoionization cross section of species i at a selected photon energy $(\sigma_i(E))$, and the mass discrimination factor (D_i) has to be accounted for:

$$S_i(T,E) \propto X_i(T)\,\sigma_i(E)\,D_i \qquad \text{eq S1}$$

At a well-defined temperature, eq S1 can be transformed to eq S2 and S3 essentially expressing the relationship between the mole fraction of species i and j,

$$\frac{S_i(T,E)}{S_j(T,E)} = \frac{X_i(T)}{X_j(T)}\frac{\sigma_i(E)}{\sigma_j(E)}\frac{D_i}{D_j} \qquad \text{eq S2}$$

$$\frac{X_i(T)}{X_j(T)} = \frac{S_i(T,E)}{S_j(T,E)}\frac{\sigma_j(E)}{\sigma_i(E)}\frac{D_j}{D_i} \qquad \text{eq S3}$$

The branching ratios R_i of the products can be then computed via eq S4:

$$R_i = \frac{X_i}{\Sigma X_i} \qquad \text{eq S4}$$

The mass discrimination factors were taken from ref [13] and determined to be $(m_i)^{0.51\,\pm\,0.11}$.

In this work, the final branching ratios (mean) were determined by taking into account mass spectra at selected photoionization energies of 9.5, 10.0, 10.5 (from PIE scans) and 15.4 eV. The data obtained at 15.4 eV used to calculate the branching ratios of methane, hydrogen and

acetylene. For multicomponent m/z peaks, the resultant $\sigma(E)$ at a particular photoionization energy has been weighted from the fitted PIE curve as the following equation.

$$\sigma_{resultant}(E) = \frac{\sum \sigma_i(E) S_i(T,E)}{\sum S_i(T,E)}$$ eq S5

Photoionization cross sections (Mb) of individual species at selected energies exploited for the calculations of the branching ratios are presented in Supplementary Table 3.

Supplementary Table 3: Photoionization cross sections (Mb) of individual species at selected energies used for the calculations of the branching ratios.
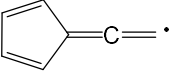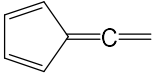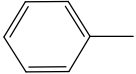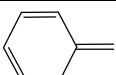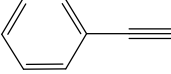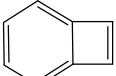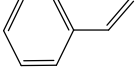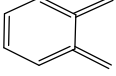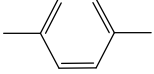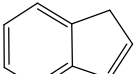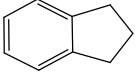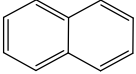
Mass	Molecular formula	Name	Photon Energy (eV)				Ref
			9.5	10.0	10.5	15.4	
2	H_2	Hydrogen	-	-	-	4.7	14
16	CH_4	Methane	-	-	-	23.85	15
26	C_2H_2	Acetylene	-	-	-	47.4	16
28	C_2H_4	Ethylene	-	-	0.92	-	15
29	C_2H_5	Ethyl	4.36	5.05	5.52	-	17
40	C_3H_4	Allene	-	5.66	15.48	-	18
		Methylacetylene	-	-	23.06	-	15
42	C_3H_6	Propene	-	5.33	9.05	-	19
52	C_4H_4	Vinylacetylene	0.4	24.36	32.45	-	20
54	C_4H_6	1,3-Butadiene	8.48	13.96	16.44	-	21
56	C_4H_8	1-Butene	-	7.35	10.02	-	19
65	C_5H_5	Cyclopentadienyl	4.59	7.99	10.03	-	22
66	C_5H_6	1,3-Cyclopentadiene	15.92	21.83	29.71	-	22
68	C_5H_8	Cyclopentene	6.53	11.21	12.68	-	20
		1,3-Pentadiene	12.71	17.24	20.56	-	18
77	C_6H_5	Phenyl	12.05	14.86	28.92	-	23
78	C_6H_6	Benzene	11.05	24.28	31.81	-	20
		Fulvene	7.06	8.33	9.16	-	23

Mass	Molecular formula	Name					
80	C_6H_8	1,3-Cyclohexadiene	18.27	22.46	27.73	-	21
		1,4-Cyclohexadiene	21.17	19.09	22.49	-	23
92	C_7H_8	Toluene	19.09	25.99	31.23	-	24
		5-Methylene-1,3-cyclohexadiene	7.02	13.51	15.24	-	23
102	C_8H_6	Phenylacetylene	28.97	51.88	62.82	-	24
104	C_8H_8	Styrene	26.28	32.15	42.89	-	24
106	C_8H_{10}	p-xylene	0.24	21.46	36.06	-	24
116	C_9H_8	Indene	27.48	39.81	52.12	-	24
118	C_9H_{10}	Indane	18.57	26.32	33.27	-	24
128	$C_{10}H_8$	Naphthalene	20.17	29.37	51.18	-	23

Supplementary Table 4: Comparison of the branching ratios (%) of the products at full decomposition of *exo*-tetrahydrodicyclopentadiene (*exo*-$C_{10}H_{16}$) with and without TiAlB NP.

Mass	Molecular formula	Name	Structure	*exo*-$C_{10}H_{16}$/ He at 1600 K[12] (%)	*exo*-$C_{10}H_{16}$/ He/TiAlB at 1050 K (%)
2	H_2	Hydrogen	H-H	5.90	1.50
15	CH_3	Methyl	$CH_3^•$	3.27	-
16	CH_4	Methane	CH_4	-	1.40
26	C_2H_2	Acetylene	$HC \equiv CH$	1.86	3.60
27	C_2H_3	Vinyl	$H_2C = CH^•$	0.24	-
28	C_2H_4	Ethylene	$H_2C = CH_2$	0.24	0.35
29	C_2H_5	Ethyl	$H_3C - CH_2^•$	0.68	-
39	C_3H_3	Propargyl	$HC \equiv C - CH_2^•$	0.85	-
40	C_3H_4	Allene	$H_2C = C = CH_2$	5.24	1.73
		Methylacetylene	$HC \equiv C - CH_3$	2.46	5.10
41	C_3H_5	Allyl	$H_2C = CH - CH_2^•$	5.02	-

42	C$_3$H$_6$	Propene	H$_2$C=CH-CH$_3$	0.93	7.03
50	C$_4$H$_2$	Diacetylene		0.06	-
52	C$_4$H$_4$	Vinylacetylene		0.23	0.11
		1,2,3-Butatriene		0.05	-
54	C$_4$H$_6$	1,3-Butadiene		3.07	3.44
56	C$_4$H$_8$	1-Butene		0.10	0.50
		2-Butene		0.03	-
64	C$_5$H$_4$	Ethynylallene		0.05	-
65	C$_5$H$_5$	Cyclopentadienyl		5.58	0.92
66	C$_5$H$_6$	1,3-Cyclopentadiene		18.62	24.11
68	C$_5$H$_8$	Cyclopentene		1.13	2.70
		1,3-Pentadiene	H$_2$C=CH—C(H)=CH—CH$_3$	0.64	3.67
77	C$_6$H$_5$	Phenyl		-	0.70
78	C$_6$H$_6$	Benzene		7.57	27.10
		Fulvene		7.24	2.14
80	C$_6$H$_8$	1,3-Cyclohexadiene		0.20 @ 1500 K	0.12
		1,4-Cyclohexadiene		0.31 @ 1500 K	0.05
82	C$_6$H$_{10}$	Cyclohexene		0.05	-

89	C_7H_5	Fulvenallenyl		0.04	-
90	C_7H_6	Fulvenallene		0.21	-
92	C_7H_8	Toluene		0.43	7.20
		5-Methylene-1,3-cyclohexadiene		0.49	1.12
102	C_8H_6	Phenylacetylene		0.01	-
		Benzocyclobutene		0.01	-
104	C_8H_8	Styrene		0.20	3.42
		o-Xylylene		0.03	-
106	C_8H_{10}	p-xylene		0.09	1.88
		1,3,5-Cyclooctatriene		0.06	-
116	C_9H_8	Indene		0.02	0.04
118	C_9H_{10}	Indane		0.06	0.05
128	$C_{10}H_8$	Naphthalene		-	0.05
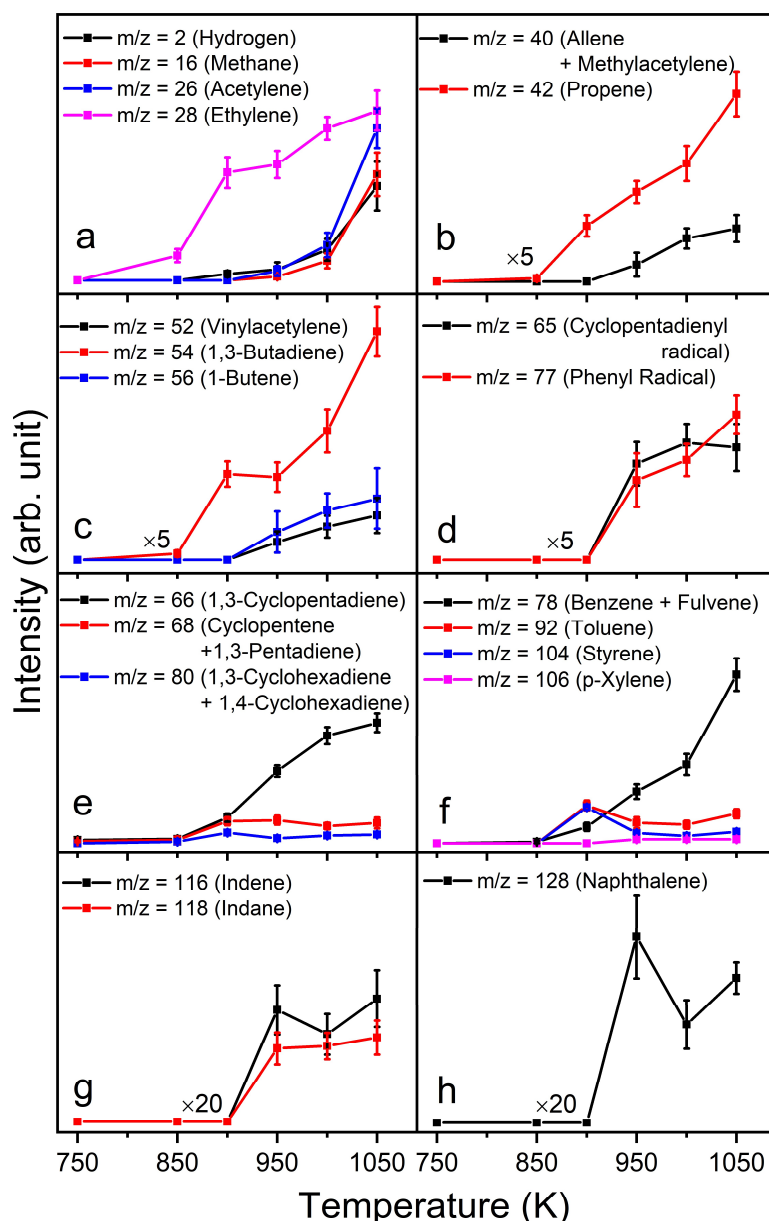
Supplementary Fig. 11: Temperature-dependent relative abundances of the products extracted from mass spectra. Mass spectra recorded at (a) 15.4 eV and (b)-(h) 10.0 eV are used to genarate the profiles. The species are grouped as – (a) hydrogen and 1C, 2C- hydrocarbons, (b) 3C- hydrocarbons, (c) 4C- hydrocarbons, (d) radicals, (e) 5C, 6C- non-aromatic hydrocarbons, (f) 6C, 7C, 8C- benzenoid hydrocarbons, (g) 9C- hydrocarbons and (h) 10C- aromatic hydrocarbon. Error bars of the *y*-axis originate from experimental errors of the mass peak intensities evaluated by averaging the mass spectra. Different colors (*black*, *red*, *blue* and *magenta*) are used to distinguish the temperature-depent abundance profiles for individual mass peaks.
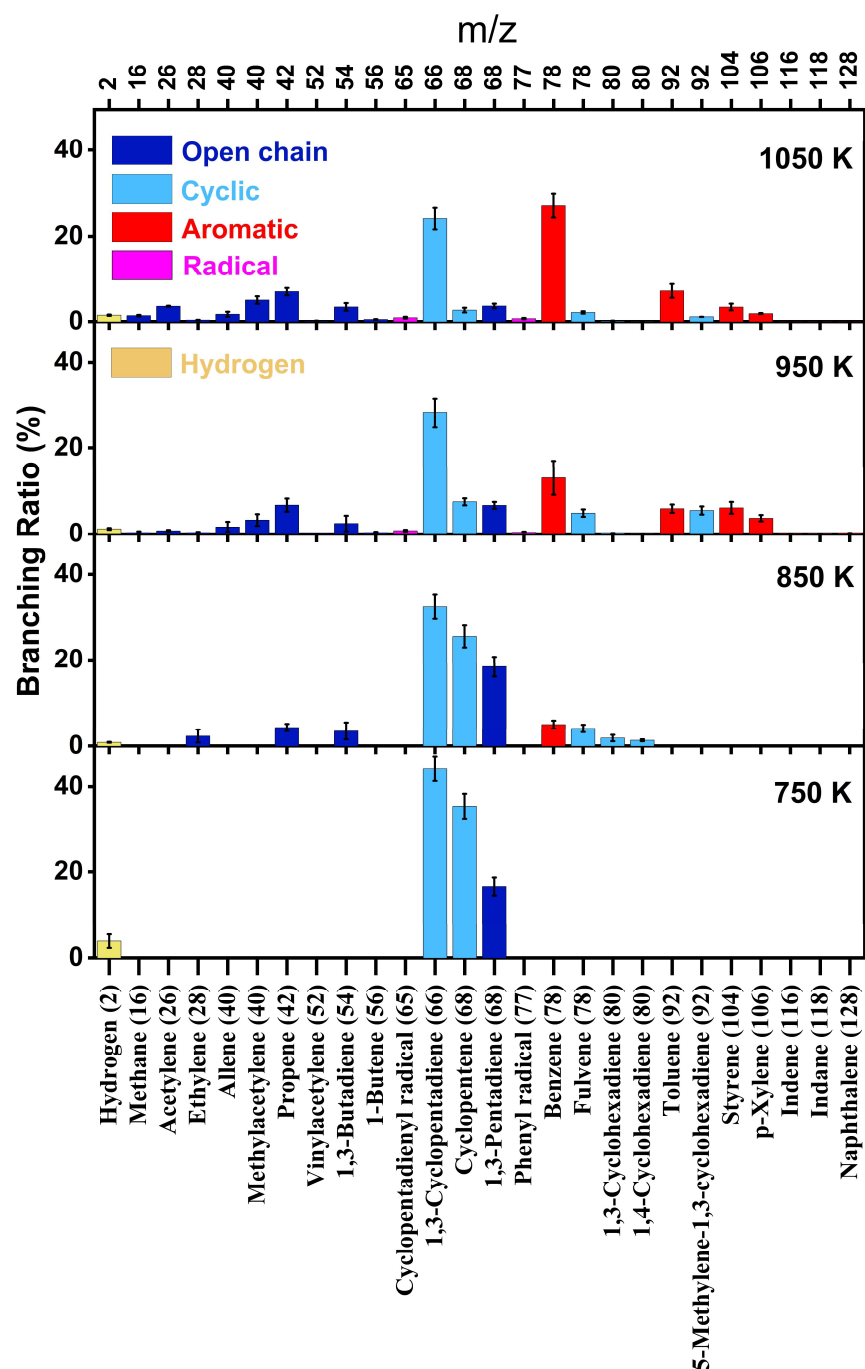
Supplementary Fig. 12: Temperature-dependent branching ratios of individual products. Quantitative determination of product distribution at particular temperatures – 750, 850, 950 and 1050 K. Overall the hydrocarbon products belong to the class of open chain (*royal blue*), cyclic (*sky blue*), aromatic (*red*), open-shell radicals (*pink*) and molecular hydrogen (*mustard yellow*). The error bars are evolved due to the uncertainties determined by averaging the recorded photoionization efficiency curves.

Supplementary Discussion 3. Geometry of TiAl₂B₆ global minimum: In the global minimum geometry (1), the largest atom in the structure, Ti, is in one of the vertices of the hexagonal TiB_5 moiety (Fig. 5). The five B atoms of TiB_5 are quasi-planar, while the Ti atom resides upward at an angle of 15° from the B_5 plane. The remaining B atom is positioned approximately in the center of TiB_5, but dipped below at an angle of 11° with respect to the B_5 plane. In the distorted hexagonal structure of TiB_5, the B-Ti-B bond angle is predicted to be 90°, while the B-B and Ti-B bond lengths are computed in the range of 157 – 161 pm and 206 – 217 pm, respectively. One of the Al atoms is situated on the top of TiB_5 moiety, perpendicular to the 'off-plane' B atom, completing the asymmetric hexagonal bipyramidal motif. The mean Al-B bond length connecting with the five B atoms in the hexagonal framework is 245 pm. The exterior Al-atom is connected directly to either of B atoms adjacent to Ti, similar to the *ortho* position in benzenoid systems and is located above the hexagonal TiB_5 ring; this generates two stereoisomers where the shortest Al-B bond length is predicted to be 214 pm. The 'on top' Al atom of $TiAlB_6$ motif is slightly shifted from the center toward the opposite side of the exterior Al atom to accommodate the steric effects on the same face of the ring.

(8)	(9)	(10)
0.439	*0.183*	*0.113*
(11)	(12)	(13)
0.110	*0.105*	*0.050*
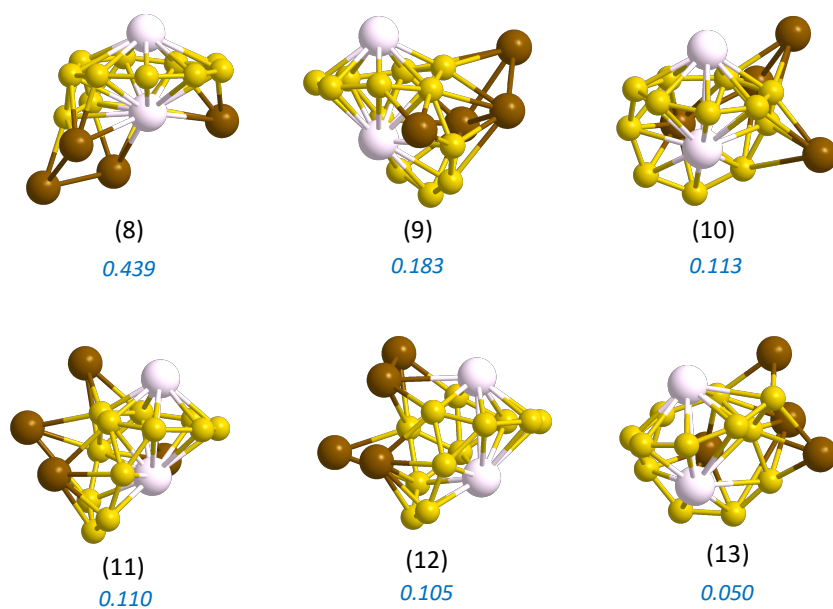
Supplementary Fig. 13: Dimeric model clusters. Structures of model $Ti_2Al_4B_{12}$ clusters (8-13) with the corresponding Boltzmann population at 750 K (sky blue) with respect to the global minimum structure (8).
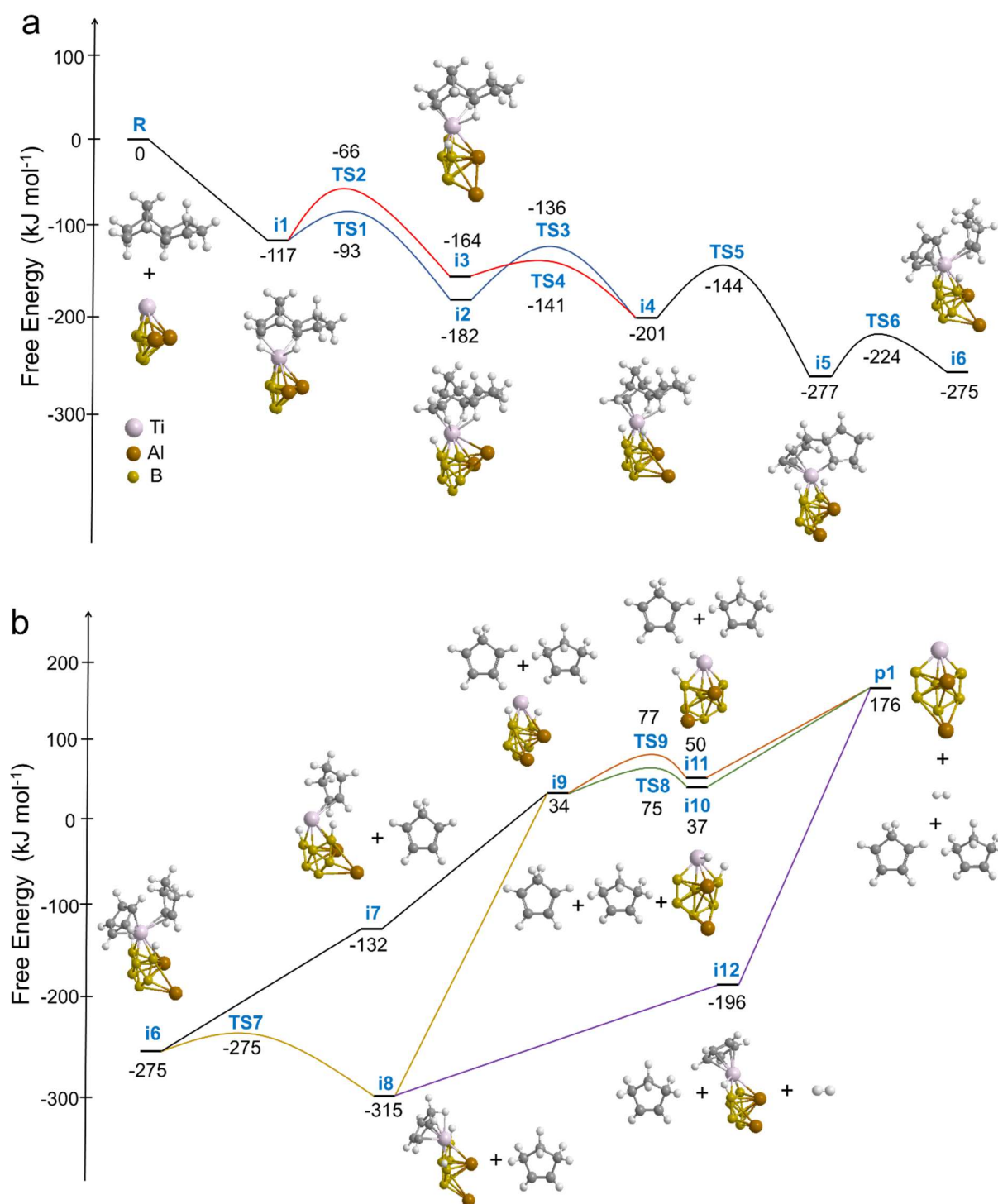
Supplementary Fig. 14: Free energy profile of the catalytic cycle at 0 K. Free energies of the intermediates (**i**) and transition states (**TS**) in the catalytic decomposition of *exo*-$C_{10}H_{16}$ on the global minimum structure of modeled TiAlB cluster (structure 1 in Fig. 5) at 0 K. The geometries of the **TS**'s are represented in Supplementary Fig. 15.
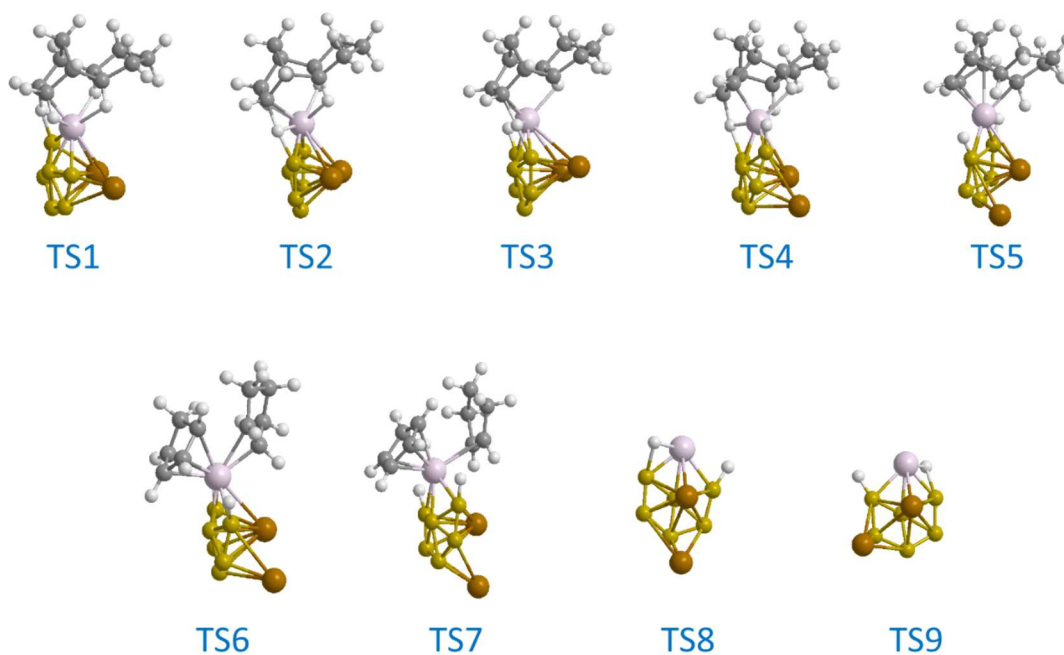
Supplementary Fig. 15: Geometries of the transition states (TS's). These **TS**'s are depicted in the free energy diagrams in Supplementary Fig. 14 and Fig. 7.

i7 to i9 NEB

i8 to i9 NEB
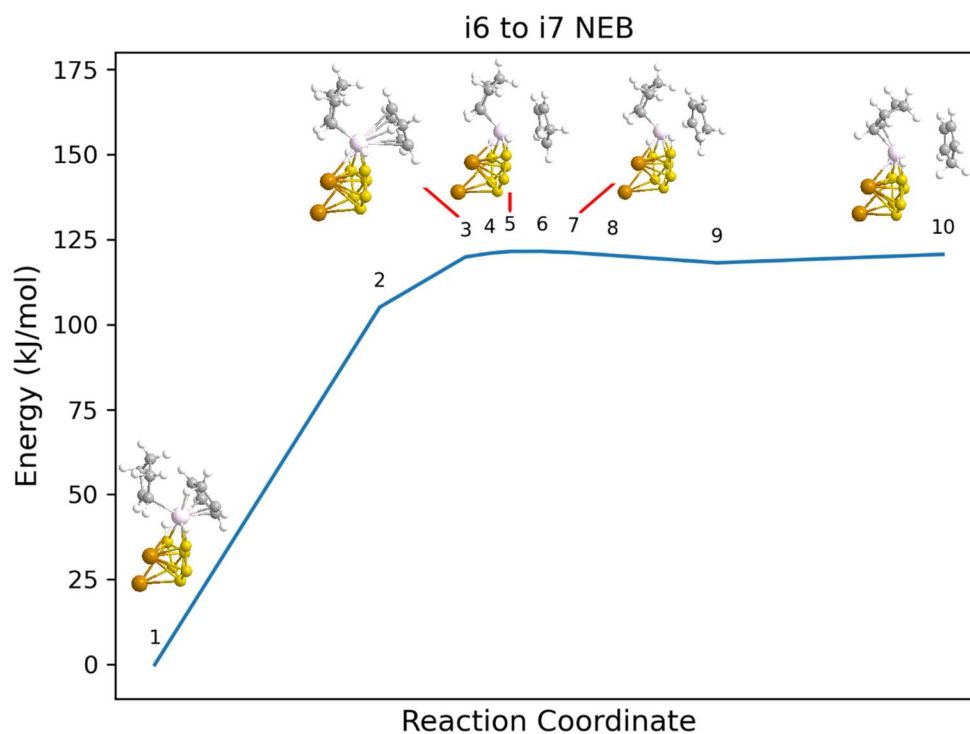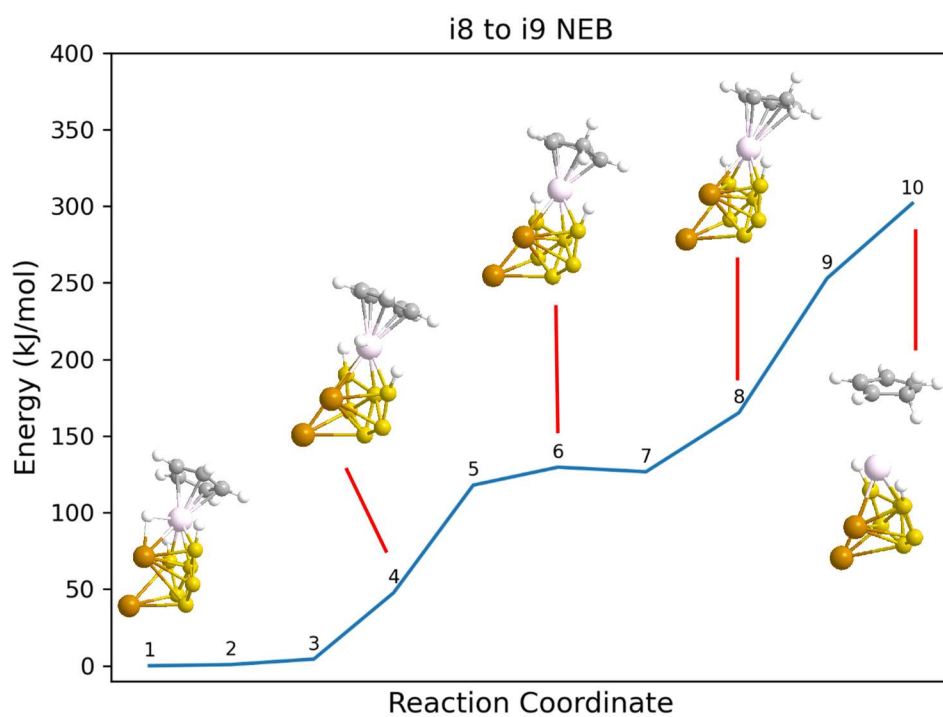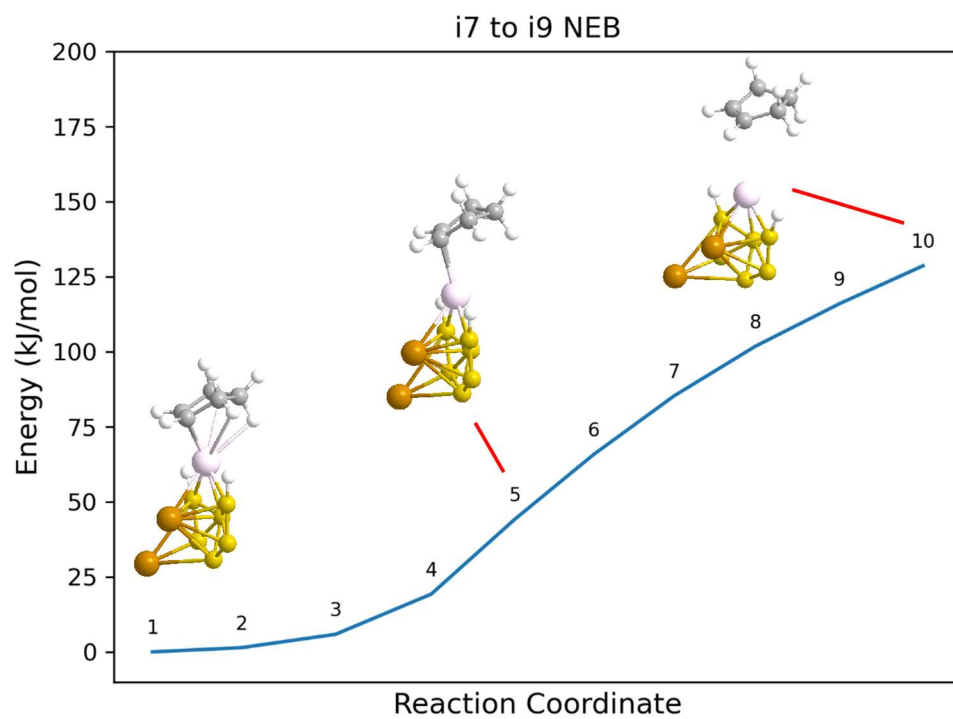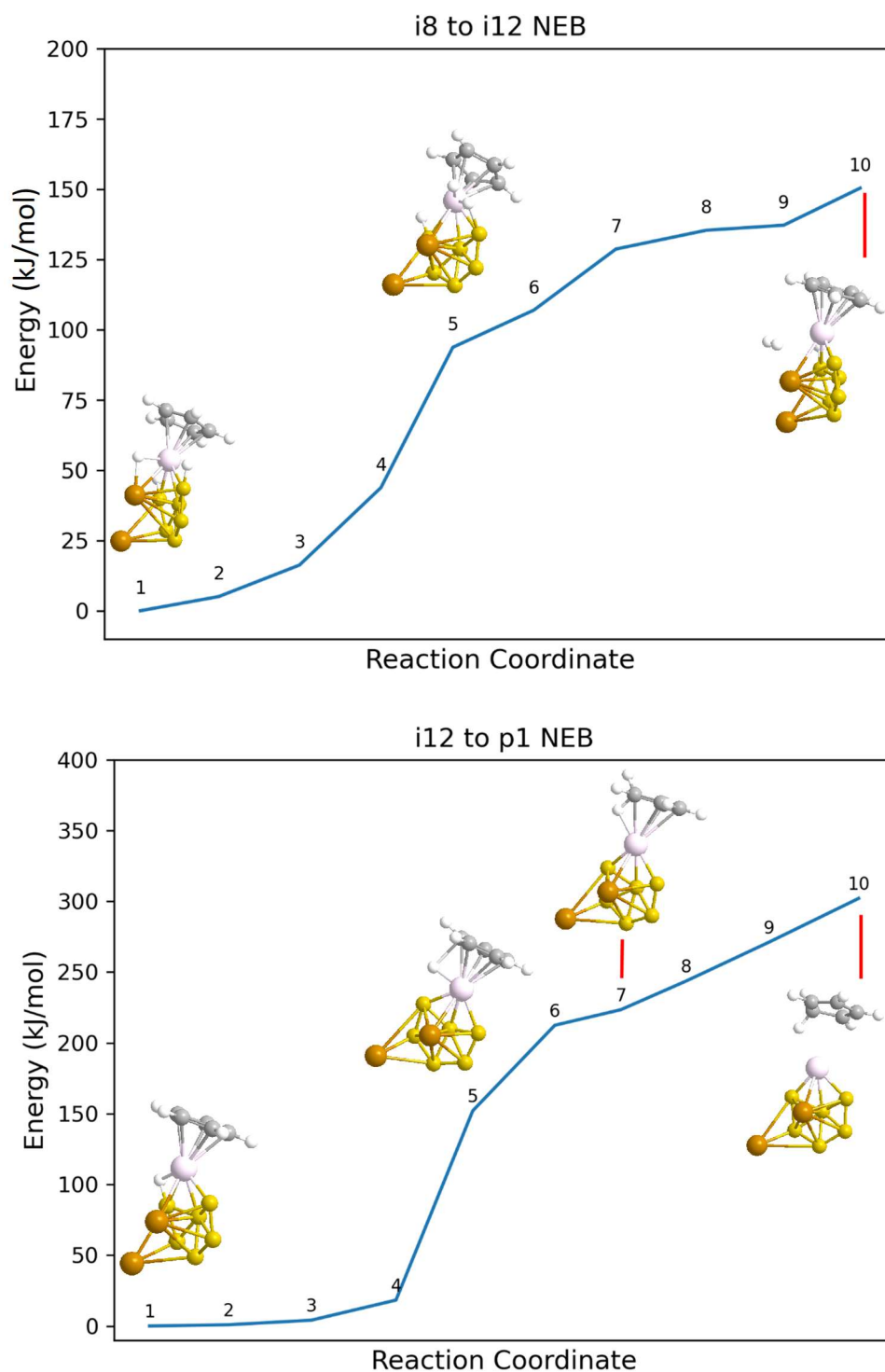
Supplementary Fig. 16: Selected enthalpic energy profiles for connected intermediates (and products). Uphill enthalpic energy profiles of certain steps in Fig. 7 and Supplementary Fig. 14 calculated by nudged elastic band (NEB) method.
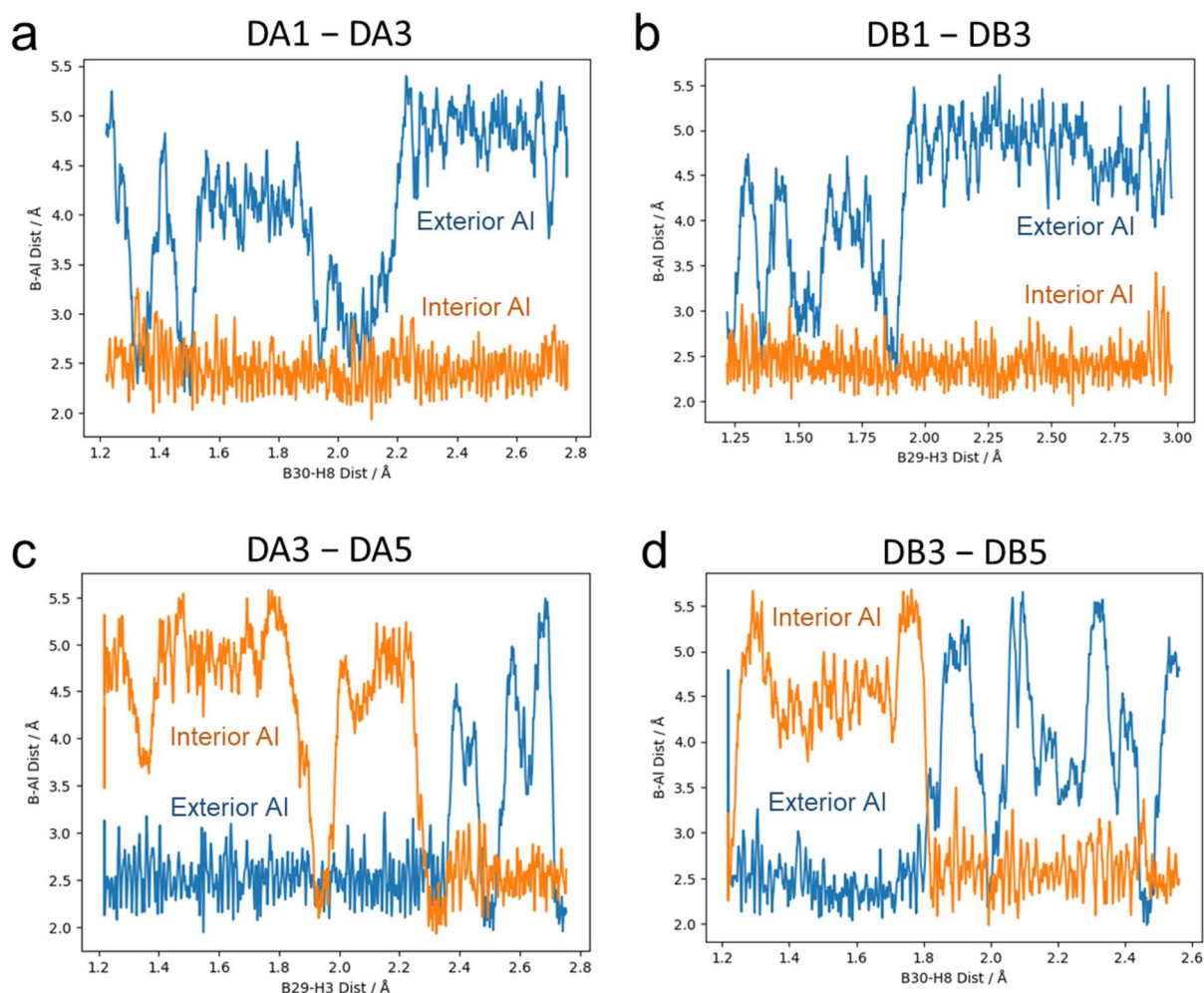
Supplementary Fig. 17: *Ab initio* **molecular dynamics simulation reveals fluxionality of Al-atoms during dehydrogenation steps.** Each plot shows the distances of the two Al-atoms (*sky blue*: exterior Al, *orange*: interior Al as referenced at intermediates DA3, DB3) from the H-atom-receiving B-center as a function of the newly forming B-H reaction coordinate. For the first H-transfer, the interior Al-atom (one cupped by the six B-atoms) is always ~2.5 Å away, while the exterior Al-atom is highly fluxional. The trajectories corresponding to the second H-transfer show that the two Al-atoms switch which one coordinates with the six B-atoms for stablization.

Supplementary References:

1. Ekoi, E. J., Gowen, A., Dorrepaal, R. & Dowling, D. P. Characterisation of titanium oxide layers using Raman spectroscopy and optical profilometry: Influence of oxide properties. *Results Phys.* **12**, 1574-1585, (2019).

2. Wang, S. *et al.* Study on the Infrared and Raman spectra of Ti3AlB2, Zr3AlB2, Hf3AlB2, and Ta3AlB2 by first-principles calculations. *Sci. Rep.* **14**, 15030, (2024).

3. Jensen, J. O. Vibrational frequencies and structural determination of aluminum tetrahydroborate. *Spectrochim. Acta A Mol. Biomol. Spectrosc.* **59**, 1565-1578, (2003).

4. Wdowik, U. D., Twardowska, A. & Rajchel, B. Vibrational spectroscopy of binary titanium borides: First-principles and experimental studies. *Adv. condens. Matter Phys.* **2017**, 4207301, (2017).

5. Lee, A. Y. *et al.* Development of the NIST X-ray photoelectron spectroscopy (XPS) database, version 5. *Data Sci. J.*, (2024).

6. Wagner C. D., Naumkin, A. V., Kraut-Vass, A., Allison, J. W., Powell, C. J., Jr. Rumble, J.R. NIST Standard Reference Database 20, Version 3.4 (web version) (http:/srdata.nist.gov/xps/) (2003).

7. Biesinger, M. C. *et al.* Quantitative chemical state XPS analysis of first row transition metals, oxides and hydroxides. *J. Phys. Conf. Ser.* **100**, 012025, (2008).

8. Biesinger, M. C. *et al.* Resolving surface chemical states in XPS analysis of first row transition metals, oxides and hydroxides: Cr, Mn, Fe, Co and Ni. *Appl. Surf. Sci.* **257**, 2717-2730, (2011).

9. Biswas, S. *et al.* Efficient oxidative decomposition of jet-fuel exo-tetrahydrodicyclopentadiene (JP-10) by aluminum nanoparticles in a catalytic microreactor: An online vacuum ultraviolet photoionization study. *J. Phys. Chem. A* **128**, 1665-1684 (2024).

10. Pimenta, M. A. *et al.* Studying disorder in graphite-based systems by Raman spectroscopy. *Phys. Chem. Chem. Phys.* **9**, 1276-1290, (2007).

11. Zhang, C. C., Hartlaub, S., Petrovic, I. & Yilmaz, B. Raman Spectroscopy characterization of amorphous coke generated in industrial processes. *ACS Omega* **7**, 2565-2570, (2022).

12. Zhao, L. *et al.* A vacuum ultraviolet photoionization study on high-temperature decomposition of JP-10 (exo-tetrahydrodicyclopentadiene). *Phys. Chem. Chem. Phys.* **19**, 15780-15807 (2017).

13. Urness KN*, et al.* Pyrolysis of furan in a microreactor. *J. Chem. Phys.* **139**, 124305 (2013).

14. Backx C, Wight GR, Wiel MJVd. Oscillator strengths (10-70 eV) for absorption, ionization and dissociation in H_2, HD and D_2, obtained by an electron-ion coincidence method *J. Phys. B: At. Mol. Phys.* **9**, 315 (1976).

15. Samson JAR, Haddad GN, Masuoka T, Pareek PN, Kilcoyne DAL. Ionization yields, total absorption, and dissociative photoionization cross sections of CH_4 from 110 to 950 Å. *J. Chem. Phys.* **90**, 6925-6932 (1989).

16. Hatano Y. Interaction of photons with molecules – cross-sections for photoabsorption, photoionization, and photodissociation. *Radiat. Environ. Biophys.* **38**, 239-247 (1999).

17. Gans B*, et al.* Absolute Photoionization Cross Section of the Ethyl Radical in the Range 8–11.5 eV: Synchrotron and Vacuum Ultraviolet Laser Measurements. *J. Phys. Chem. A* **115**, 5387-5396 (2011).

18. Yang B, Wang J, Cool TA, Hansen N, Skeen S, Osborn DL. Absolute photoionization cross-sections of some combustion intermediates. *Int. J. Mass Spectrom.* **309**, 118-128 (2012).

19. Koizumi H. Predominant decay channel for superexcited organic molecules. *J. Chem. Phys.* **95**, 5846-5852 (1991).

20. Cool TA, Wang J, Nakajima K, Taatjes CA, McLlroy A. Photoionization cross sections for reaction intermediates in hydrocarbon combustion. *Int. J. Mass Spectrom.* **247**, 18-27 (2005).

21. Wang J, Yang B, Cool TA, Hansen N, Kasper T. Near-threshold absolute photoionization cross-sections of some reaction intermediates in combustion. *Int. J. Mass Spectrom.* **269**, 210-220 (2008).

22. Hansen N*, et al.* Identification of C5Hx Isomers in fuel-rich flames by photoionization mass spectrometry and electronic structure calculations. *J. Phys. Chem. A* **110**, 4376-4388 (2006).

23. Photonionization Cross Section Database (Version 2.0); National Synchrotron Radiation Laboratory; Hefei, China, http://flame.nsrl.ustc.edu.cn/database/.

24. Zhou Z, Xie M, Wang Z, Qi F. Determination of absolute photoionization cross-sections of aromatics and aromatic derivatives. *Rapid Commun. Mass Spectrom.* **23**, 3994-4002 (2009).